



Influence mechanism of process parameters on the interfacial characterization of selective laser melting 316L/CuSn10

Jie Chen, Yongqiang Yang^{*}, Changhui Song^{**}, Di Wang, Shibiao Wu, Mingkang Zhang

School of Mechanical & Automotive Engineering, South China University of Technology, Guangzhou, China

ARTICLE INFO

Keywords:

Selective laser melting
Multi-material
Bimetallic structure
Interfacial characterization
Mechanical properties

ABSTRACT

Bimetallic structures can combine the performance of dissimilar metal materials to meet the multifunctional requirement in industrial solutions. In this paper, steel-bronze bimetallic structures were fabricated via self-developed multi-material selective laser melting (SLM) equipment. In order to investigate the influence of laser power, scanning speed, and hatching space on the interfacial characterization, three factors and five levels of orthogonal experiments were performed on twenty layers of CuSn10 tin bronze after forming the 316 L stainless steel. Optical microscope (OM), large depth field microscope, scanning electron microscopy (SEM), energy dispersive spectroscopy (EDS), tensile properties, electron backscattering diffraction (EBSD) and nano-indentation were used to characterize these bimetallic structures to validate the impact from process parameters. The large depth field microscope revealed protrusions at the steel/bronze interface, and its height increased and then decreased with increasing volumetric energy input. Besides, the generation of interfacial defects is related to the interfacial process parameters, and it is found that the types of defects are mainly classified as holes and cracks. Insufficient energy will cause cracks in the horizontal direction and then lead to bonding failure. Conversely, higher energy input will generate microcracks in the vertical direction. The defects near the interfacial region are the main factors affecting the ultimate strength of the bonding strength. As a result, the steel-bronze bimetallic structure displays optimal joint ultimate strength of 459.54 ± 3.08 MPa with elongation of $5.23 \pm 0.65\%$, and minimum joint ultimate strength of 199.02 ± 0.56 MPa with elongation of $1.70 \pm 0.22\%$. Their fracture morphology also exhibited gully-like and fan-shaped features, respectively. Additionally, the EBSD results show that there are fine grain regions appeared in the interfacial region, which helps increase the average nano-hardness of the interfacial region. This study provides a reference for the influence of process parameters on the interfacial characterization and mechanical properties of steel-bronze bimetallic parts prepared by selective laser melting.

1. Introduction

Additive manufacturing (AM) is an emerging field and has recently gained significant attention in industry and academia. AM methods highlights several advantages compared to traditional methods, such as rapid prototyping, personalized customization and higher flexibility in terms of achievable geometries. So far, many scholars are committed to conferring the AM methods' advantages to the manufacturing of multi-material structures [1–4]. Bimetallic structures are typical multi-material structure fabricated by joining dissimilar metals and have customized mechanical, physical and chemical properties, such as hardness, electrical conductivity, magnetic permeability, corrosion

resistance and thermal conductivity [5–7]. Compared with single-material structure, bimetallic structure with multiple functions can provide unique solutions to engineering problems [8,9]. In the past, traditional methods to combine two different metal materials were usually to adapt welding, rolling, diffusion bonding and powder metal-allurgy technology, etc. [10–16]. However, most of them are limited to specific shape and material, high manufacturing costs, or suboptimal bonding strength. Conversely, bimetallic structure made by AM can be designed in multiple shapes, and the smaller process thermal stress is also conducive to the improvement of interfacial bonding force. (see Fig. 16)

The AM methods for bimetallic structures mainly include laser

^{*} Corresponding author.

^{**} Corresponding author.

E-mail addresses: meiqyang@scut.edu.cn (Y. Yang), song_changhui@163.com (C. Song).

<https://doi.org/10.1016/j.msea.2020.139316>

Received 22 January 2020; Received in revised form 19 March 2020; Accepted 26 March 2020

Available online 2 April 2020

0921-5093/© 2020 Elsevier B.V. All rights reserved.

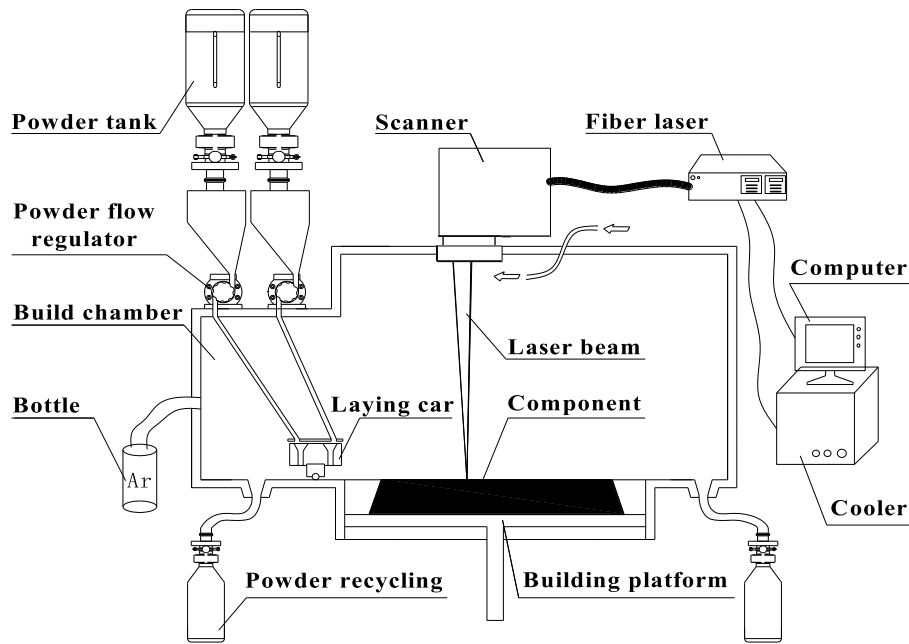


Fig. 1. Schematic of the multi-material SLM machine.

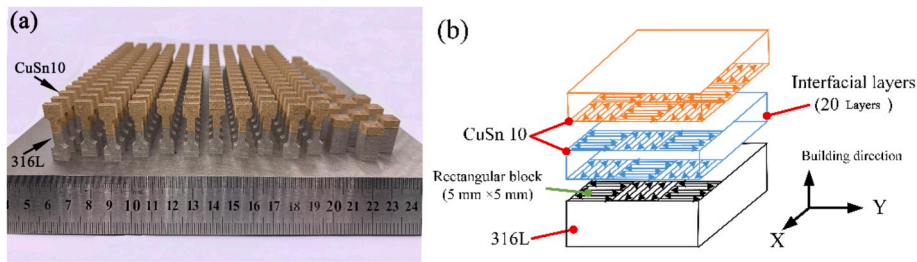


Fig. 2. (a) 316L/CuSn10 bimetallic structure fabricated by Dimetal-300, (b) inter-layer staggered scanning strategy and island scanning strategy.

Table 1
Process parameters of 316 L SS and CuSn10 TB.

	316 L SS	CuSn10 TB
Laser power (W)	200	300
Scanning speed (mm/s)	1200	700
Scanning space (mm)	0.07	0.085
Layer thickness (mm)	0.03	0.03
Relative density (%)	98.68	98.66

Table 2
Three factors and five levels.

Factor level	Laser power/(W)	Scanning speed/(mm/s)	Hatching space/(mm)
1	260	500	0.075
2	280	600	0.08
3	300	700	0.085
4	320	800	0.09
5	340	900	0.095

powder bed fusion (L-PBF) technology [17,18] and laser directed energy deposition (L-DED) technology [19,20]. The L-PBF technology exhibit further advantages such as the formation of finer geometries, internal channels, and lattice structures [21]. In contrast, L-DED processes have higher deposition rates and the flexibility to reshape on the existing structural components. By adding multiple powder feeders connected to

Table 3
Orthogonal experimental design of interfacial layers.

Experiment no.	Laser power/(W)	Scanning speed/(mm/s)	Hatching space/(mm)
1	260	500	0.075
2	260	600	0.08
3	260	700	0.085
4	260	800	0.09
5	260	900	0.095
6	280	500	0.08
7	280	600	0.085
8	280	700	0.09
9	280	800	0.095
10	280	900	0.075
11	300	500	0.085
12	300	600	0.09
13	300	700	0.095
14	300	800	0.075
15	300	900	0.08
16	320	500	0.09
17	320	600	0.095
18	320	700	0.075
19	320	800	0.08
20	320	900	0.085
21	340	500	0.095
22	340	600	0.075
23	340	700	0.08
24	340	800	0.085
25	340	900	0.09

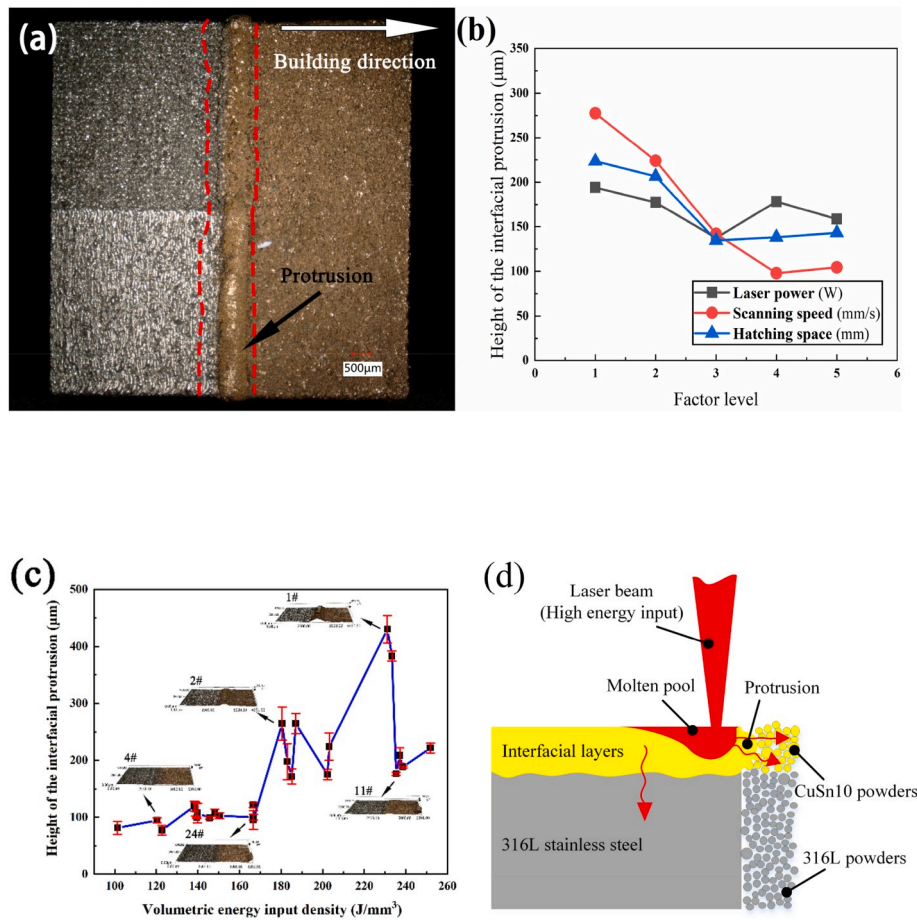


Fig. 3. (a) The picture of interfacial protrusion, (b) orthogonal experimental results, (c) the relationship between the interfacial protrusions' height and laser volumetric energy input density, (d) the schematic diagram of protrusion's generation.

Table 4
Average values and standard deviation of the interfacial protrusions' height.

Experiment no.	Interfacial protrusions' height (µm)	Experiment no.	Interfacial protrusions' height (µm)
1	430.23 ± 24.18	14	121.55 ± 4.26
2	264.51 ± 28.95	15	114.27 ± 12.16
3	99.00 ± 3.60	16	208.63 ± 13.64
4	94.71 ± 4.21	17	264.39 ± 17.43
5	81.56 ± 11.60	18	223.97 ± 24.09
6	383.18 ± 9.10	19	95.15 ± 16.37
7	198.04 ± 31.46	20	99.31 ± 1.45
8	108.42 ± 6.39	21	188.60 ± 2.04
9	77.51 ± 8.32	22	221.64 ± 8.52
10	119.64 ± 8.60	23	175.05 ± 9.24
11	176.63 ± 2.69	24	100.16 ± 5.13
12	171.66 ± 12.92	25	107.39 ± 17.16
13	102.89 ± 4.84		

the deposition head, the original L-DED system can gain the multi-material forming capability [22]. However, converting the original L-PBF system to multi-material manufacturing is much more complicated, e.g., the selective laser melting (SLM) system is capable of multi-material forming capability by equipping a powder laying car with two powder hoppers [23–25], a pre-mixed powder device with multiple supply cylinders [26], or a powder feed nozzle device [27]. This capability within SLM system can open up to special possibilities for material and product design, such as mixing different powders at a given ratio in forming, functionally graded materials (FGM) forming, lattice and solid integration structural design.

Bronze alloy has good electrical and thermal conductivity, but low hardness and poor corrosion resistance [28]. Stainless steel has considerable hardness, strength, and good corrosion resistance [29]. Therefore, the steel-bronze bimetallic structure can effectively reduce costs and meet requirements, which has been widely used in molds, electrical contacts, and cooling components, etc. Steel and bronze have very different thermal conductivity and thermal expansion rate, which hinders the desire for a better interfacial bonding strength. In consequence, the ability to develop bimetallic structures by SLM still poses significant challenges. In previous reports, Liu et al. obtained a good metallurgical combination steel-copper bimetallic structure based on SLM [30]. Wei et al. demonstrate the fabrication of horizontal functional gradient 316L/CuSn10 components [31]. However, few studies have focused on the effect of process parameters on the direct bonding interface of the steel-bronze bimetallic structures. Hence, the paper studied the influence mechanism of process parameters on the interfacial characterization, which mainly involves interfacial surface roughness, interfacial defects, interfacial chemical composition diffusion, and interfacial ultimate tensile strength.

2. Experimental methods

2.1. Experimental materials and equipment

All parts were made on the self-developed multi-material Dimetal-300 SLM machine of the MAE school (Mechanical and Automotive Engineering) in South China University of Technology, the device schematic is shown in Fig. 1 [23]. This SLM device is equipped with an IPG YLR-400-WC Yb:YAG fiber laser, which produces a laser beam with a

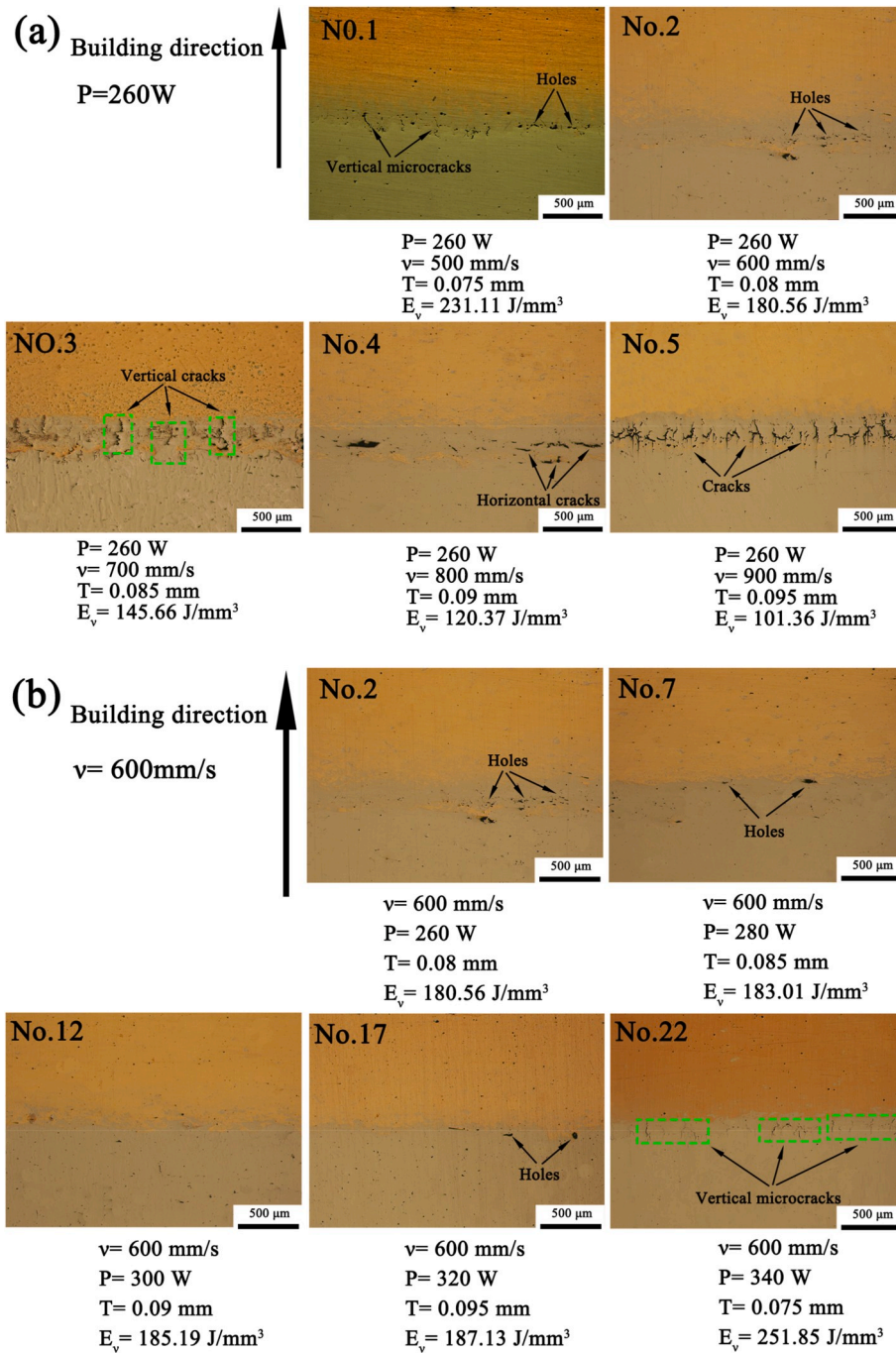


Fig. 4. Optical micrographs of interfacial defects in the steel/bronze bimetallic structures (50 ×): (a) when the laser power is 260 W, (b) when the scanning speed is 600 mm/s.

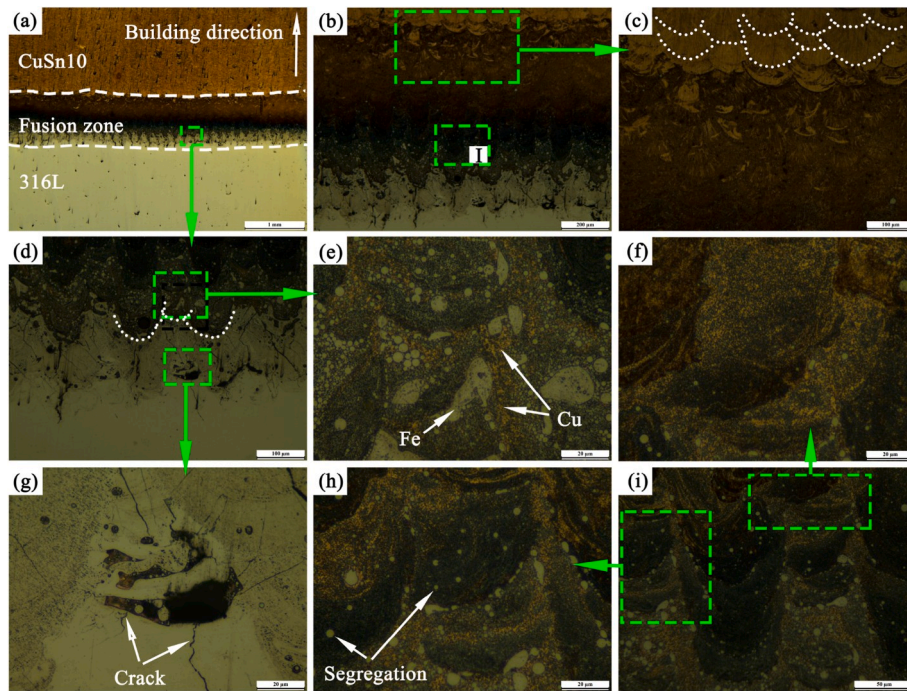


Fig. 5. The optical micrographs after etching: (a) overall region ($25\times$), (b) interfacial region ($100\times$), (c) CuSn10 TB region ($200\times$), (d) 316 L SS region ($200\times$), (e) and (g) a partially enlarged view of 316 L SS region ($1000\times$), (i) area I of interfacial region ($500\times$), (f) and (h) a partially enlarged view of area I ($1000\times$).

wavelength of 1064 nm and can reach a maximum power of 400 W. Unlike other single-material SLM equipment, a multiple powder delivery system was designed for this machine, which includes two sets of powder feeding device with a method of feeding powders from outside to inside of the build chamber. Besides, there are two powder hoppers on the laying car that can load two kinds of metal powder at the same time, and each powder hopper has a switch to control the unloading of powders. In this experiment, spherical 316 L stainless steel (316 L SS) and CuSn10 tin bronze (CuSn10 TB) alloy powders produced by gas-atomized were used. Their chemical composition and micromorphology have been investigated in previous research [23].

2.2. Experimental methods

In order to investigate the process parameters' influence on the formation of interfacial layers and the mechanical properties of joints, steel-bronze bimetallic structures shown in Fig. 2(a) were fabricated by the multi-material SLM equipment in this experiment. The optimal process parameters of individual materials have been studied in previous experiments, and the optimized results are shown in Table 1. As shown in Fig. 2(b), the inter-layer staggered scanning strategy and the island scanning strategy were applied throughout the whole SLM formation process [32], and the scanning lines were S-shaped orthogonal in the $5\text{ mm} \times 5\text{ mm}$ rectangular block. In this work, an orthogonal experiment was performed on twenty layers of CuSn10 TB after forming the 316 L stainless steel (Fig. 2(b)), and the thickness of layer is 0.03 mm. As aforementioned, three factors and five levels of orthogonal experiments were designed, as shown in Tables 2 and 3.

2.3. Macroscopic and microscopic feature

For studying the surface morphology of bimetallic samples fabricated by multi-material SLM machine, the samples' interfacial macroscopic feature was observed by a large depth field microscope (VHX-5000, Japan) first. Then, SLM samples were polished by a series of emery

sheets (600 #–2000 #), and polished by diamond polishing solution of $0.5\text{ }\mu\text{m}$ particle size and SiO_2 polishing solution of $0.05\text{ }\mu\text{m}$ particle size, respectively. The polished SLM samples were etched on the CuSn10 TB side by ferric chloride hydrochloric acid solution ($6\text{ g FeCl}_3 + 10\text{ ml HCl} + 150\text{ ml H}_2\text{O}$) for 6 s, and the interfacial microscopic feature of samples were investigated by using a Model DMi8 C Leica metallographic microscope. Besides, the element distributions in the interfacial fusion zone were analyzed by electron dispersive spectroscopy (EDS) from Oxford Instruments X-Max, and interfacial microstructure was observed by Quanta-200 SEM.

The EBSD test was used to analyze the interfacial grain orientation distribution, so the SLM samples were further polished by ion grinding and polishing instrument (Leica EM TIC 3X). EBSD test was performed on a GeminiSEM 300 SEM system (Carl Zeiss, Germany) equipped with Hikari XP EBSD detector (EDAX, USA), using a step size of $0.1\text{ }\mu\text{m}$. Moreover, the EBSD data were analyzed by using OIM analysis software.

2.4. Mechanical properties

As shown in Fig. 2(a), non-standard size tensile specimens were prepared in this experiment, and they were cut from 316 L SS substrate by wire electric discharge machining (EDM), then sanded to remove the protrusions at the interface. Tensile specimens were deformed to failure at a fixed crosshead speed of 1 mm/min by using an CMT5105 tensile machine (Zhuhai SUST Ltd, China), and three samples were tested per condition. The nanoindentation tests were performed on the SLM-formed samples by using an Agilent G200 Nano indenter (Agilent Technologies Inc, USA) equipped with a Berkovich pyramidal-shaped indenter tip. A Fused Silica reference sample was used for calibration before conducting the nanoindentation tests. From the 316 L SS region to the CuSn10 TB region, 24 points were selected for the nanoindentation test with a maximum load of 300 mN and a load time of 15s.

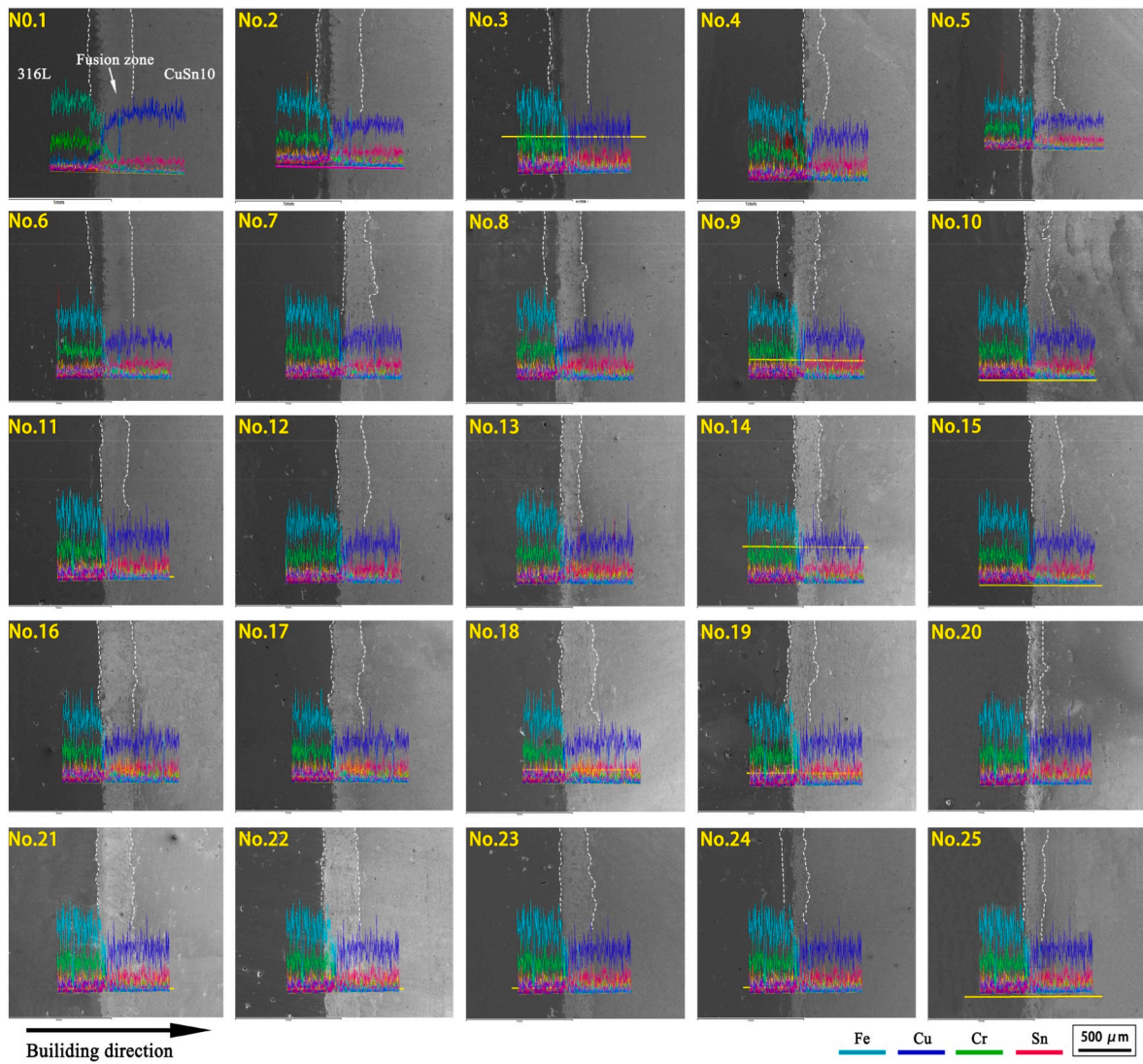


Fig. 6. The EDS analysis results of interfaces in the steel/bronze bimetallic structures.

Table 5

Average values and standard deviation of the fusion-zone's width in the steel/bronze bimetallic structures.

Experiment no.	Width of fusion zone (μm)	Experiment no.	Width of fusion zone (μm)
1	422.40 ± 6.98	14	241.30 ± 11.60
2	406.20 ± 49.89	15	309.36 ± 30.90
3	362.79 ± 12.95	16	355.76 ± 32.17
4	210.37 ± 25.45	17	269.14 ± 42.53
5	324.81 ± 17.45	18	312.45 ± 30.28
6	382.83 ± 12.28	19	203.40 ± 17.57
7	262.95 ± 39.53	20	146.17 ± 34.18
8	320.19 ± 29.63	21	324.83 ± 15.22
9	331.28 ± 19.13	22	316.32 ± 24.37
10	252.90 ± 58.83	23	256.77 ± 29.01
11	244.39 ± 10.96	24	227.73 ± 4.19
12	269.91 ± 38.29	25	180.97 ± 28.51
13	194.12 ± 25.87		

3. Results and discussions

3.1. Surface morphology of the interface

Fig. 3(a) reveals the presence of protrusions on the steel-bronze interface, and the protrusions' height were measured by a large depth field microscope. The values of protrusions' height are shown in Table 4. For studying the relationship between the protrusions' height and the interfacial process parameters, the interfacial protrusions' height was taken as the orthogonal optimization goal, and the results are shown in Fig. 3(b). According to the range analysis. It is found that the scanning speed of 179.64 has the most important influence on the interfacial protrusions' height, followed by the hatching space of 88.78, and the laser power of 56.60 is minimal. In general, the deposition rate of the SLM process is mainly related to the scanning speed and the hatching space. In this experiment, the higher the deposition rate, the faster the adhesion speed of the CuSn10 TB alloy to the 316 L SS alloy. Therefore, the faster bonding of CuSn10 TB alloy and the 316 L SS alloy is more conducive to the transfer of heat to the 316 L SS alloy (Fig. 3(d)), and less heat is transferred to the surrounding CuSn10 TB powders, resulting in a smaller protrusion height. The effect on interfacial protrusion is described by the volumetric energy input density, and the formula is as follows [33,34]:

$$E_v = \frac{P}{vTh} \tag{1}$$

Where, E_v is the laser volumetric energy input density (J/mm³), P is laser power (W), v is scanning speed (mm/s), T (mm) is hatching space (mm), h is thick layer (mm).

Therefore, Fig. 3(c) display the relationship between the interfacial protrusions' height and volumetric energy input density. The degree of interfacial undulation observed by the large depth of field microscope reflects that as the volumetric energy input density increases, the height of the interfacial protrusion approximately first increases and then decreases. This is mainly due to the difference in thermal conductivity between 316 L SS and CuSn10 TB, and the heat transfer rate between objects is directly proportional to the thermal conductivity. With the increase of the laser volumetric energy input density, more heat was transferred to the surrounding CuSn10 TB powders, which causes the surrounding bronze powders to melt and solidify to form protrusions (Fig. 3(d)). However, if the energy input density continues to increase, the gas around the molten pool will push away the bronze powders around the molten pool, so a powder-free area will be formed near the molten pool [35,36]. This is not conducive to the thermal transmission to the bronze powders around the interface.

3.2. Microscopic features

Optical micrographs of interfacial defects in the steel/bronze bimetallic structures are shown in Fig. 4, and the effects of interfacial process parameters on the defects near the interface were observed. Defect types are mainly divided into pores and cracks, and the defects degree is related to the change of laser volumetric energy input density. As shown in the photo of experimental sample No. 1 (Fig. 4(a)), holes and vertical cracks appear near the interfacial region with the laser power of 260 W and the scanning speed of 500 mm/s. However, with the increase of scanning speed and hatching space, the laser volumetric energy input density also decrease from 231.11 J/mm³ to 101.36 J/mm³, and the holes caused by incomplete melting became more and more obvious, and even horizontal cracks appeared (Fig. 4(a), No. 4), which would lead to the failure combination of 316 L SS and CuSn10 TB. Moreover, when laser scanning speed is 600 mm/s, as the laser volumetric energy input density increases from 180.56 J/mm³ to 251.85 J/mm³, the type of

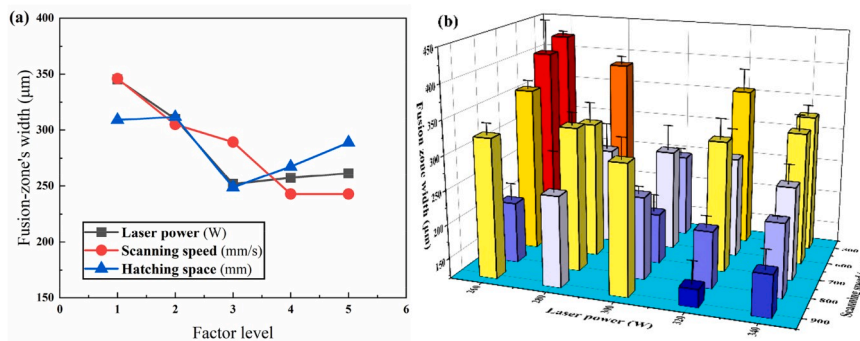


Fig. 7. (a) Orthogonal experimental results, (b) the relationship between fusion-zone's width and laser power and scanning speed.

Table 6

ANOVA results of fusion-zone's width.

Source	Sum of squares (SS)	Degree of freedom (df)	Mean squares (MS)	F-Value	significance
Laser power (W)	33442.52	4	8360.63	6.76	*
Scanning speed (mm/s)	38485.56	4	9621.39	7.77	**
Hatching space (mm)	14630.06	4	3657.51	2.96	
Error	9901.31	8	2669.85		

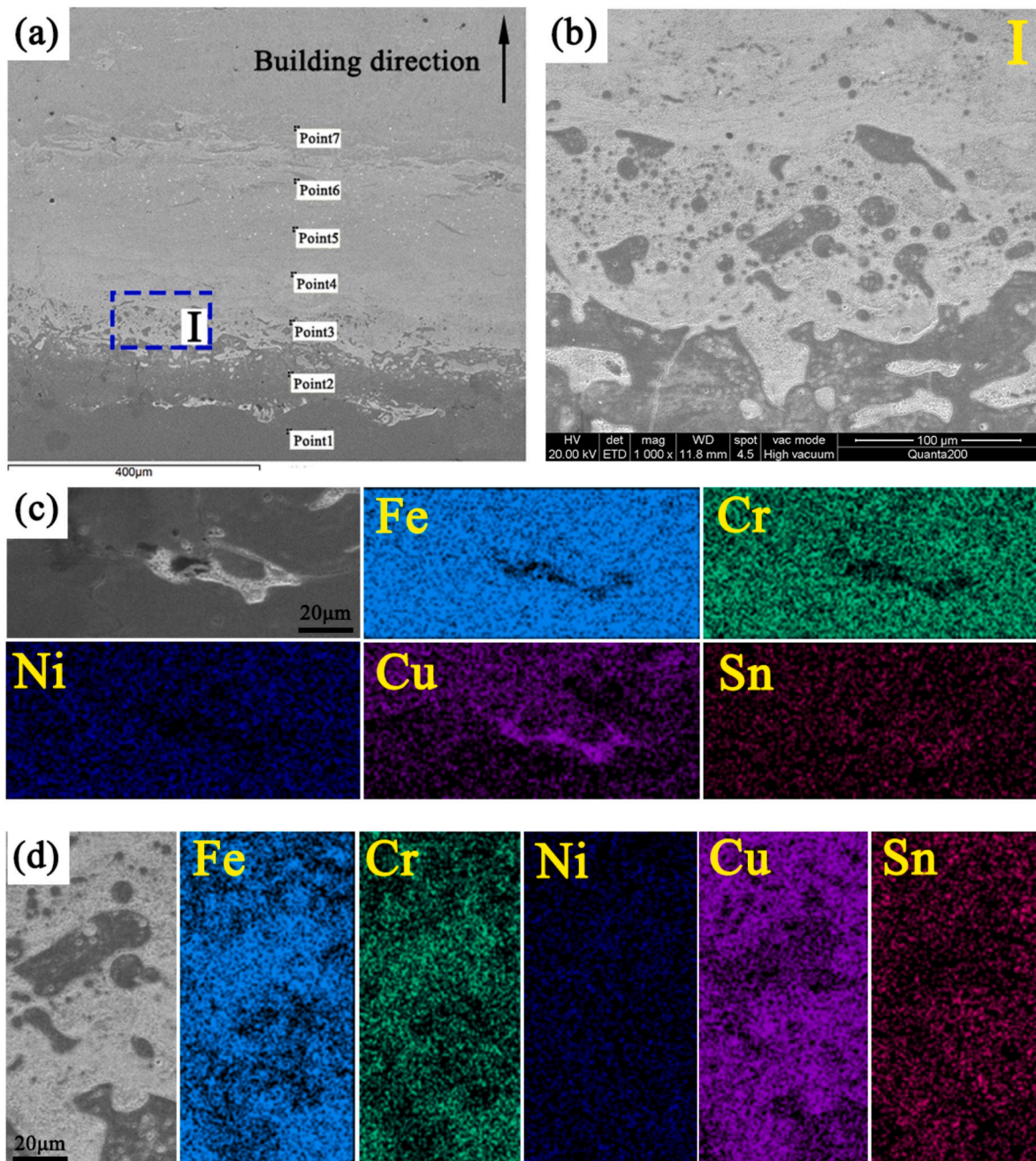


Fig. 8. Interfacial SEM images of experimental sample No. 1: (a) overall fusion zone (200 ×) and (b) area I of overall fusion zone (1000 ×); EDS mapping at (c) 316 L SS region (1000 ×) and (d) fusion-zone (1000 ×).

Table 7
Elements at spots.

Spectrum No.	Elements					
	Distance from point 1 (µm)	Fe (wt.%)	Cu (wt.%)	Cr (wt.%)	Sn (wt.%)	Others (wt.%)
Point 1	0	58.64	0.90	16.54	0	23.92
Point 2	75	45.13	18.50	12.54	1.91	21.92
Point 3	150	22.15	47.48	6.20	5.84	18.33
Point 4	225	9.15	67.44	2.58	8.17	12.66
Point 5	300	4.22	73.81	0.97	8.79	12.21
Point 6	375	2.29	76.60	0.70	8.61	11.80
Point 7	450	0.77	79.17	0	9.40	10.66

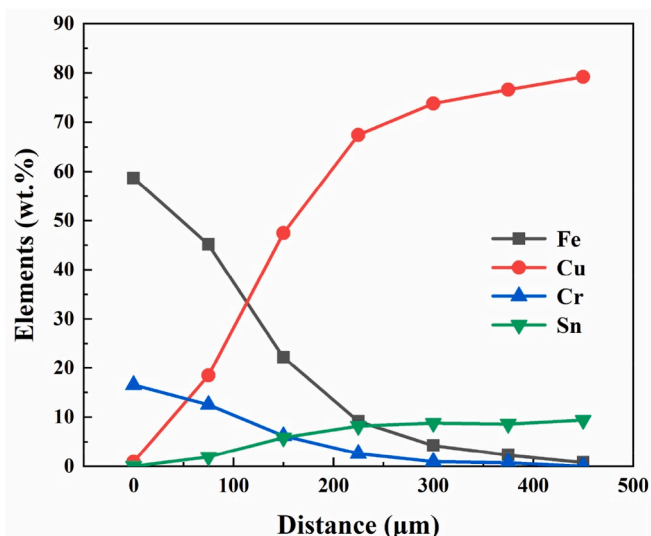


Fig. 9. Chemical composition of interface.

Table 8

Average values and standard deviation of ultimate tensile strength, elongation after fracture.

Experiment no.	Ultimate tensile strength (MPa)	Elongation after fracture (%)
1	402.55 ± 12.86	2.27 ± 0.38
2	328.88 ± 2.68	1.93 ± 0.11
3	374.64 ± 23.99	1.97 ± 0.16
4	242.75 ± 18.29	1.74 ± 0.16
5	215.49 ± 23.71	1.52 ± 0.21
6	373.53 ± 31.65	2.12 ± 0.29
7	280.69 ± 27.10	1.50 ± 0.09
8	213.00 ± 33.28	1.59 ± 0.18
9	212.97 ± 55.51	2.73 ± 0.38
10	330.02 ± 32.09	1.78 ± 0.24
11	288.52 ± 11.38	1.94 ± 0.02
12	441.54 ± 12.01	4.42 ± 0.38
13	390.02 ± 64.17	2.17 ± 0.08
14	459.54 ± 3.08	5.23 ± 0.65
15	234.42 ± 44.48	1.78 ± 0.01
16	274.18 ± 43.68	1.79 ± 0.09
17	199.02 ± 0.56	1.70 ± 0.22
18	282.3 ± 8.39	1.41 ± 0.01
19	253.61 ± 23.18	1.63 ± 0.11
20	247.57 ± 27.82	1.57 ± 0.21
21	204.12 ± 38.76	2.00 ± 0.13
22	259.09 ± 3.35	1.77 ± 0.12
23	357.27 ± 11.82	2.12 ± 0.37
24	282.68 ± 5.16	1.57 ± 0.40
25	354.83 ± 0.51	2.54 ± 0.12

defect changes from holes to microcracks (Fig. 4(b)). Therefore, Fig. 4 reveals that the increasing of volumetric energy input density from 101.36 J/mm³ to 251.85 J/mm³ promotes melting completely, thereby reducing the occurrence of interface defects. In consequence, the types of defects developed from horizontal cracks to holes, and to vertical cracks, then to microcracks and pores.

Furthermore, the experimental sample No. 1 was etched and analyzed for interfacial microscopic features. As shown, the “layer-layer” and “track-track” molten pool boundaries were revealed in the CuSn10 region, which were marked by white dash-dotted line in Fig. 5 (c). However, due to the weak corrosion effect of ferric chloride hydrochloric acid solution on 316 L SS, with the increasing of Cu element, different degrees of corrosion appeared on the fusion-zone. Also, the boundary of molten pools near the fusion-zone were marked by white dash-dotted line (Fig. 5(d)), revealing that a steel region surrounded by Cu element area was found in the center of the molten pool (Fig. 5(e)). In

general, Cu and Fe atoms have similar atomic radii, crystal structures, and lattice constants, making it easy to form replacement solid solutions in liquid state [37,38]. Thereby, due to the higher density of bronze (8.8 g/cm³) than steel (7.98 g/cm³) and the Marangoni convection [39], the steel was pulled toward the molten pool center from the border of molten pool. At the same time, the bronze was flowing into the border and contained in the Fe matrix due to the high cooling rate of the border. As shown in Fig. 5(g), the microcracks grow from the hole. Besides, minute bronze areas were observed within the hole in the 316 L SS region. Moreover, the region I of interfacial region was further observed in Fig. 5 (i), which is close to the CuSn10 TB region. Fig. 5(h) shows the segregations of droplet-like steel in the steel-bronze solid solution, which mainly caused by the limited mutual solubility of steel and bronze in the solid state. As aforementioned, the droplet-shaped steel areas were precipitated from a supersaturated solution of bronze with the decreasing of temperature.

3.3. The element diffusion on the interface

As shown in Fig. 6, the interface of steel/bronze bimetallic structure can be distinguished as three areas: 316 L SS region, fusion zone and CuSn10 TB region. Thereby, the diffusion distance of elements under different interfacial process parameters was analyzed by using EDS test. The fusion-zone’s width was summarized in Table 5, which shows that the maximum width of the fusion zone is 422.40 ± 6.98 μm and the minimum is 146.17 ± 34.18 μm. Moreover, in order to study the influence of interfacial process parameters on the fusion-zone’s width, the fusion-zone’s width was taken as the target of the orthogonal experiment, and the results are shown in Fig. 7(a). According to the range analysis, the scanning speed of 103.23 has the most important influence on the fusion-zone’s width, followed by the laser power of 93.50, and the hatching space of 62.90 is minimal. As shown, the fusion-zone’s width decreased as the increasing of scanning speed. In Table 6, for given significance level α of 0.01 ($F_{0.01}(4, 8) = 7.01$) or 0.05 ($F_{0.05}(4, 8) = 3.84$), only scanning speed has a very significant effect on the experimental results, and laser power has a significant effect on the experimental results, and hatching space has no significant effect on the experimental results. This indicates that the fusion-zone’s width is mainly related to the liquid time of the molten pool, and the smaller the scanning speed, the longer the diffusion time of the elements. Also, Fig. 7 (b) shows that the maximum fusion-zone’s width is obtained at lower laser power and scanning speed.

Fig. 8 shows the interfacial microstructure of experimental sample No. 1, and its elements’ distribution was analyzed. As shown in Fig. 8(a), seven points were selected at the same interval (75 μm) across the interfacial direction to determine the chemical composition. Table 7 shows the chemical composition results for point analysis. The point 1 is located on the 316 L SS region with 58.64% Fe and 0.9% Cu, and point 7 is located on the CuSn10 TB region with 0.77% Fe and 79.17% Cu. Moreover, the change curves of chemical composition are shown in Fig. 9, indicating that both the increasing rate of Cu elemental content and the decreasing rate of Fe elemental content were increase first and then decrease. Besides, Fig. 8(c) shows that concentrated distribution of the bronze in the 316 L SS region, and Fig. 5(e) shows the concentrated distribution of the stainless steel in the CuSn10 TB region. This is consistent with the results obtained in Fig. 5(e).

3.4. Tensile properties

Tensile tests were used to characterize the interfacial bonding strength of steel/bronze bimetallic structure, and a summary of the tensile properties are presented in Table 8. All tensile specimens were broken at the interface. Thereby, the steel-bronze bimetallic structure displays optimal joint ultimate strength of 459.54 ± 3.08 MPa with elongation of 5.23 ± 0.65% (Table 8, No.14), and minimum joint ultimate strength of 199.02 ± 0.56 MPa with elongation of 1.70 ± 0.22%

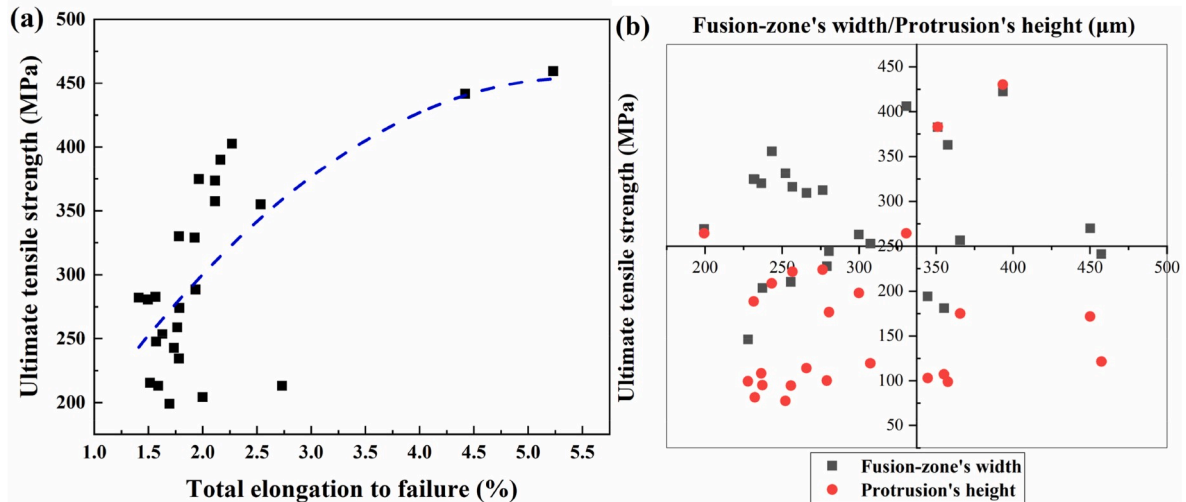


Fig. 10. (a) Ultimate tensile strength vs. total elongation to failure for steel/bronze bimetallic structure, (b) scatter plot of the ultimate tensile strength and the fusion-zone's width and protrusions' height.

(Table 5, No.17). Moreover, it can be understood that the defects near the interfacial region are the main factors affecting the ultimate strength of the bonding strength. Therefore, the experimental samples of no.4 and no.5 separately show joint ultimate strength of 242.75 ± 18.29 MPa and 215.49 ± 23.71 MPa with elongation of $1.74 \pm 0.16\%$ and $1.52 \pm 0.21\%$, which all have the defects of holes and horizontal cracks as shown in Fig. 4(a) (N0.4 and No.5). Interestingly, the cracks in the direction perpendicular to the interface seem to have little effect on the bonding strength of the joint. As shown, the experimental sample of no.1 has a considerable joint ultimate strength of 402.55 ± 12.86 MPa. Incidentally, the joint strength of welded steel/copper tensile specimens is approximately 200 MPa, which is reported in these references [40–43]. Fig. 10(a) compares the ultimate tensile strength vs. total elongation to failure for steel/bronze bimetallic structure fabricated by selective laser melting. There is a general positive growth relationship between ultimate tensile strength and elongation, which indicates that the higher the ultimate tensile strength, the greater the elongation after fracture. As shown, Fig. 10(b) displays the scatter plot of the fusion-zones' width, the height of the protrusions, and the ultimate tensile strength. It reveals that the joint ultimate tensile strength of most samples is below 350 MPa. Additionally, Fig. 10(b) shows that a larger joint bonding strength can be obtained when the fusion-zone's width is at a medium value, and the smaller protrusion's height is also beneficial to obtain high joint bonding strength.

The fracture morphologies of the tensile test specimens with the maximum and minimum joint ultimate tensile strength are shown in Fig. 11 and Fig. 12, respectively. In Fig. 11(g) and (h), the fracture surface of the tensile samples is uneven, and there are many steep cliffs on the bronze fracture surface. Moreover, two typical fracture morphologies appear on steel fracture surface of the experimental sample No. 14, such as the smooth surface in Fig. 11(d) and the gully-like features in Fig. 11(e). Fig. 11(f) shows that the fracture occurred after the section was torn into small pieces, and there were cleavage steps near the crack. A balling features was found on the steel fracture surface in Fig. 11(c), and many secondary cracks appeared near it, indicating that the inclusions had caused vertical cracks to occur before the component fractured. In contrast, fracture surface of the experimental sample No. 17 is flusher as shown in Fig. 12(a) and (e). Compared with Fig. 11(e), the fracture morphology of Fig. 12(c) is mainly fan-shaped cleavage patterns, which may mainly originate from inclusions, that is, a large amount of unmelted powders shown in Fig. 12(f). Interestingly, dimple characteristics were found on the surface of the steel fracture in Fig. 12(d). In addition, many tongue-like patterns were observed in Fig. 12(g),

and cleaving steps were also found in Fig. 12(h).

3.5. EBSD analysis

The grain distribution of steel/bronze bimetallic specimen (experimental N0. 10) was observed by EBSD technology, and the EBSD detector view is the side surface of the sample. The XYZ directions of the sample's coordinate system are: laser scanning direction (TD), building direction (BD) and normal direction (ND) of the sample's side surface. It was reported that cubic system is the main crystal structure in the 316 L SS, CuSn10 TB and their interface in these references [21,23,31,44]. As shown in Fig. 13(a), the columnar crystals were found in the grain orientation map of CuSn10 TB region, and the growth direction of the columnar crystals is approximately along the BD direction. This is mainly due to the temperature gradient formed along the BD direction and the high thermal conductivity of the bronze. Because only crystal nuclei with a growth direction parallel to the temperature gradient direction can grow quickly, and when the crystal nuclei encounter adjacent crystal grains, the growth stops and columnar crystal grains are formed. Besides the BD direction, temperature gradient is also generated between the border and center of molten pool. Thereby, the approximate position of the molten pool boundaries (marked by dotted line in Fig. 13(b)) can be deduced from the growth direction of bronze columnar crystals, that is, the long axis direction of the columnar crystal (Fig. 13(c)).

Fig. 13(b) shows the EBSD orientation map of the interfacial zone between the 316 L SS region and the fusion zone, indicating that the grain size of the fusion zone is much smaller than that of the steel region. The area I of Fig. 13(b) was further observed in Fig. 13(c), revealing that fine grains appear near the border of the molten pool. These fine grains may be formed for two reasons. On the one hand, the mixing of multiple elements in the fusion zone may promote a large increase in the number of crystal nuclei and significantly refine the grains [45]. On the other hand, the absolute temperature generated by the laser beam at the border of the molten pool is much lower than the center of the molten pool, which results in insufficient time for the crystal nuclei to grow. In addition, it can be found that the grains with $\langle 001 \rangle$ preferential orientation are filled in red color as shown in Fig. 13(b), and the maximum value of texture intensity is 8.793 based on the IPF (Fig. 14(b)). The inverse pole figures (Fig. 14(b)) also shows that the $\langle 001 \rangle$ orientation is parallel to the ND direction of the sample's side surface. Besides, the $\langle 101 \rangle$ preferred orientation parallel to the BD and TD direction of the sample's side surface was also found in IPFs (Fig. 14(b)).

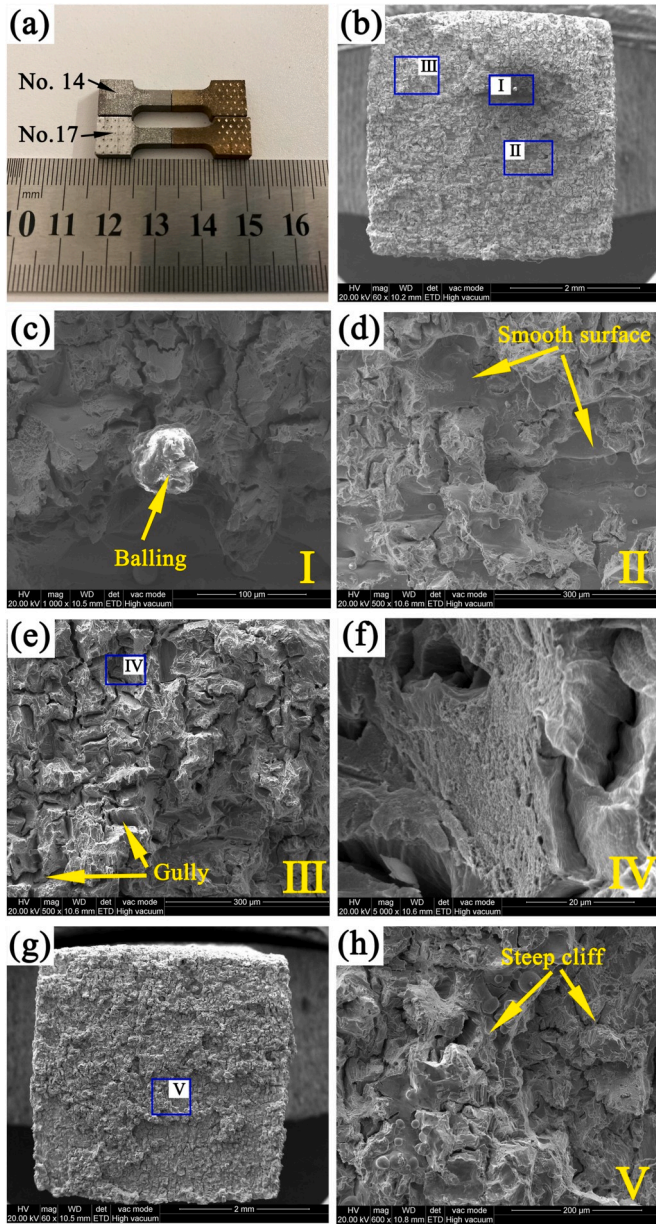


Fig. 11. (a) Picture of experimental sample No. 14 and No. 17, fracture morphologies of experimental sample No. 14: (b) SEM micrograph of entire steel fracture ($60\times$), (c) area I of entire steel fracture ($1000\times$), (d) area II of entire steel fracture ($500\times$), (e) area III of entire steel fracture ($500\times$), (f) area IV of (e) ($5000\times$), (g) SEM micrograph of entire bronze fracture ($60\times$), (h) area V of entire bronze fracture ($600\times$).

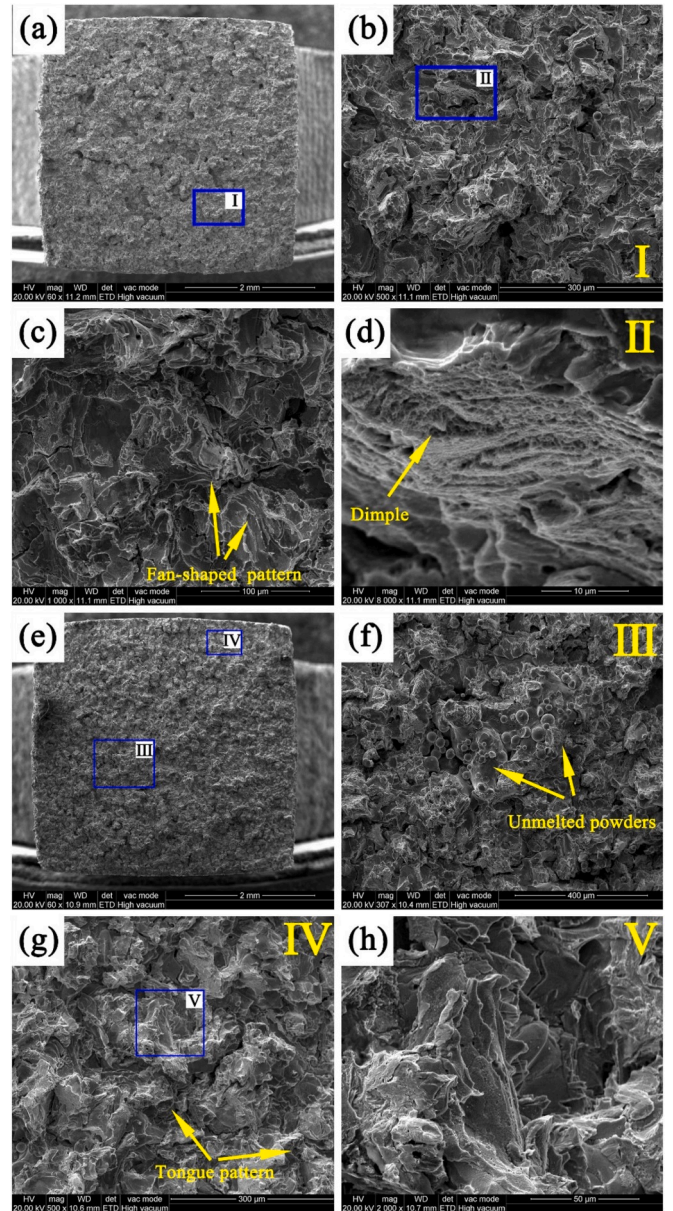


Fig. 12. Fracture morphologies of experimental sample No. 17: (a) SEM micrograph of entire steel fracture ($60\times$), (b) area I of entire steel fracture ($500\times$), (c) enlarged view of entire steel fracture ($1000\times$), (d) area II of (b) ($8000\times$), (e) SEM micrograph of entire bronze fracture ($60\times$), (f) area III of entire bronze fracture ($300\times$), (g) area IV of entire bronze fracture ($500\times$), (h) area V of (g) ($2000\times$).

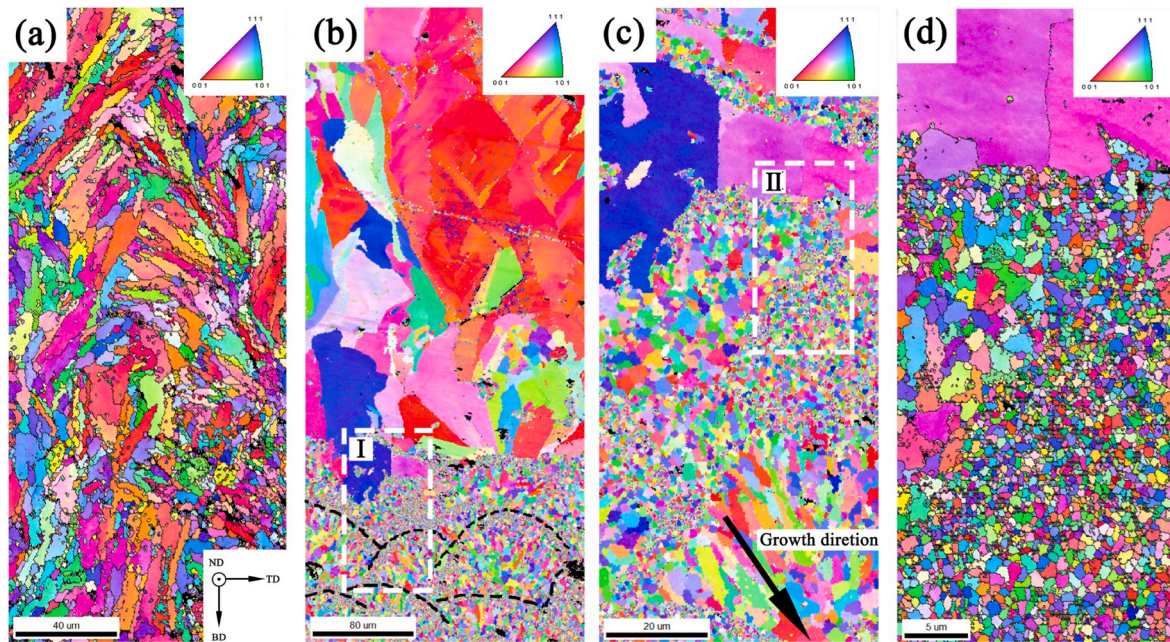


Fig. 13. The grain orientation of steel/bronze bimetallic samples fabricated by SLM: (a) CuSn10 TB region, (b) the area between the 316 L SS region and the fusion zone, (c) area I of (b), (d) area II of (c).

This phenomenon was also observed in the study of SLM-formed CoCrMo by Xin et al [46]. As shown in Fig. 14(c) and (d), the characteristic of the crystal's $\langle 001 \rangle$ preferred orientation parallel to the ND direction with maximum texture intensity of 2.432 is also found in the CuSn10 TB region. Therefore, the temperature gradient formed in the ND and TD directions also lead to preferred orientations of the crystal grains [47](see Fig. 15).

3.6. Nanoindentation test

Nano-hardness was conducted for understanding the hardness change across the interfacial region. Select points from the steel region to the bronze region with a pitch of 50 μm , and the values of nano-hardness and young's modulus were summarized in Table 9. The 316 L SS region shows average nano-hardness of 2.61 ± 0.09 GPa with young's modulus of 128.68 ± 1.95 GPa, and CuSn10 TB region shows average nano-hardness of 2.03 ± 0.11 GPa with young's modulus of 94.81 ± 2.82 GPa. There values are close to that reported in other researches [48–50]. Obviously, the interfacial region shows average nano-hardness of 2.97 ± 0.36 GPa with young's modulus of 111.78 ± 10.49 GPa, which is a bit larger than the nano-hardness in the steel region. Wei et al. also found this phenomenon in the reference [31]. This is related to the fine grain region in Fig. 13(b), refining the grains can increase the hardness of the material. However, the value of young's modulus didn't increase in the interfacial region. Generally, young's modulus reflects the ability of solid material to resist deformation. Therefore, the results indicate that a harder solid solution phase may be present in the interfacial region.

4. Conclusions

In this paper, the 316L/CuSn10 bimetallic structures were fabricated by a self-developed multi-material SLM equipment, and the effects of process parameters on the formation of interfacial layers and the mechanical properties of joints were investigated. The following conclusions can be drawn:

- (1) Due to the difference in heat transfer coefficient between steel and bronze, interfacial protrusions occurred and the scanning speed has the most important effect on the interfacial protrusions' height. With the increase of the volumetric energy input density, the interfacial protrusions' height increased first and then decreased. Additionally, the generation of interfacial defects is related to the laser volume energy input density. Insufficient laser energy input density will cause incomplete melting of the interfacial layer, which will lead to the generation of holes and horizontal cracks. Conversely, excessive laser energy input density can cause vertical microcracks and pores.
- (2) The fusion-zone's width shows a maximum value of 422.40 ± 6.98 μm and a minimum value of 146.17 ± 34.18 μm . Based on the results of the variance analysis, only scanning speed has a very significant effect on the fusion-zone's width, and laser power has a significant effect on it, and hatching space has no significant effect on it. This reveals that the liquid retention time of the molten pool is the dominant factor in element diffusion during the SLM processing.
- (3) The results of tensile tests show that the steel-bronze bimetallic structure displays optimal joint ultimate strength of 459.54 ± 3.08 MPa with elongation of $5.23 \pm 0.65\%$, and minimum joint ultimate strength of 199.02 ± 0.56 MPa with elongation of $1.70 \pm 0.22\%$. The defects near the interfacial region were the main factors affecting the joint ultimate strength of the bonding strength. Moreover, when the fusion-zone's width is at a medium value or the protrusions' height is smaller, a higher bonding strength can be obtained.
- (4) The fine grain areas in the interfacial region were found by EBSD analysis, and they were mainly distributed at the border of the molten pool. This is mainly related to the increase of nucleation rate caused by multi-element mixing and the large undercooling on the molten pool boundary. Besides, the nanohardness reaches an average maximum value of 2.97 ± 0.36 GPa at the interfacial region, which is related to the fine grains in the interfacial region.

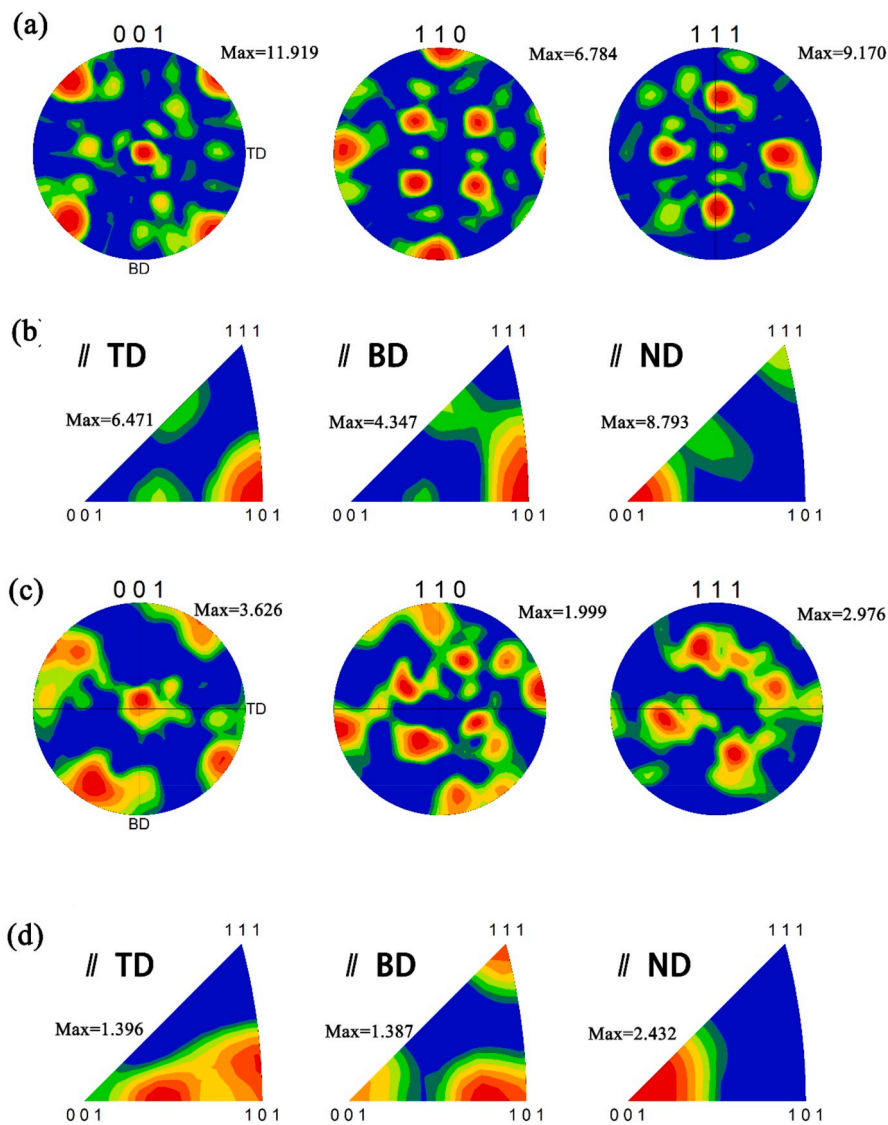


Fig. 14. (a) The pole figures and (b) the corresponding inverse pole figures of the area between the 316 L SS region and the fusion-zone (Fig. 13(b)); (c) the pole figures and (d) the corresponding inverse pole figures of the CuSn10 TB region (Fig. 13(a)).

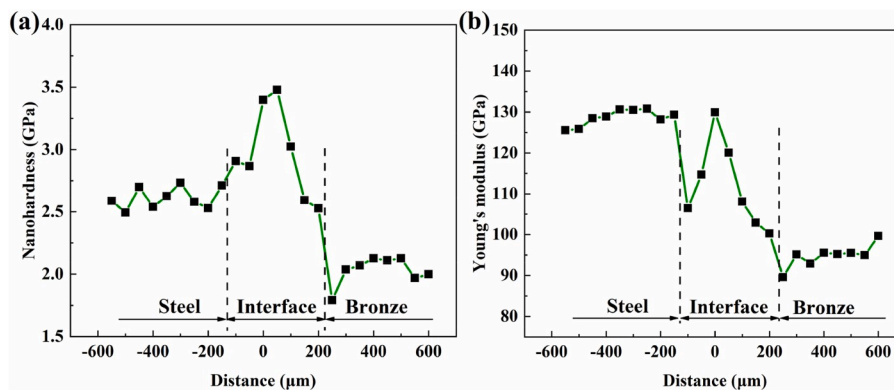


Fig. 15. (a) Nano-hardness and (b) young's modulus along the steel/bronze interface.

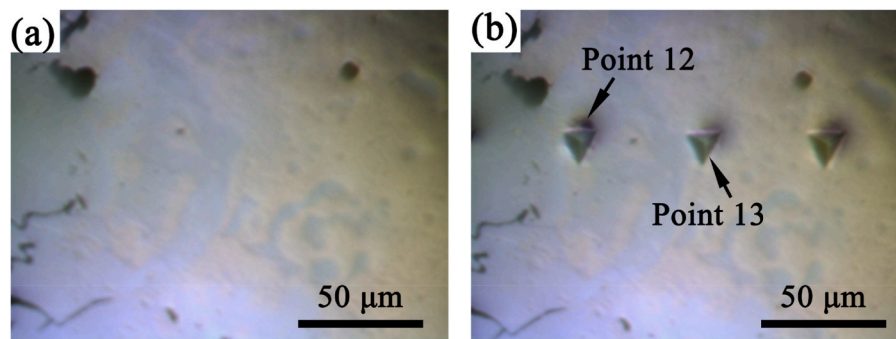


Fig. 16. The optical pictures of nanoindentation test (1000 ×).

Table 9

Average values and standard deviation of nano-hardness and Young's modulus in each region.

Region type	Nano-hardness (GPa)	Young's modulus (GPa)
Steel region	2.61 ± 0.09	128.68 ± 1.95
Interfacial region	2.97 ± 0.36	111.78 ± 10.49
Bronze region	2.03 ± 0.11	94.81 ± 2.82

Declaration of competing interest

The authors declare that they have no known competing financial interests or personal relationships that could have appeared to influence the work reported in this paper.

CRediT authorship contribution statement

Jie Chen: Conceptualization, Methodology, Investigation, Formal analysis, Writing - original draft. **Yongqiang Yang:** Funding acquisition, Project administration, Writing - review & editing. **Changhui Song:** Data curation, Writing - review & editing. **Di Wang:** Supervision, Visualization, Writing - review & editing. **Shibiao Wu:** Investigation. **Mingkang Zhang:** Investigation.

Acknowledgements

This work was funded by the Natural Science Foundation of China (NSFC, No. 51875215, No. 51705160), Guangdong Province Science and Technology Project (No. 2018B090905001, No. 2017B090911014), Guangzhou Science and Technology Project (No. 201704030097), Open Fund of National Engineering Research Center of Near-Net-Shape Forming for Metallic Materials (NO. 2019005).

References

- [1] B. Zhang, P. Jaiswal, R. Rai, S. Nelaturi, Additive manufacturing of functionally graded material objects: a review, *J. Comput. Inf. Sci. Eng.* 18 (4) (2018).
- [2] X. Zhang, C. Wei, Y.-H. Chueh, L. Li, An integrated dual ultrasonic selective powder dispensing platform for three-dimensional printing of multiple material metal/glass objects in selective laser melting, *J. Manuf. Sci. Eng.* 141 (1) (2019).
- [3] C. Shen, Z. Pan, D. Cuiuri, J. Roberts, H. Li, Fabrication of Fe-FeAl functionally graded material using the wire-arc additive manufacturing process, *Metall. Mater. Trans. B* 47 (1) (2015) 763–772.
- [4] M. Naebe, K. Shirvanimoghaddam, Functionally graded materials: a review of fabrication and properties, *Appl. Mater. Today* 5 (2016) 223–245.
- [5] B. Heer, A. Bandyopadhyay, Compositionally graded magnetic-nonmagnetic bimetallic structure using laser engineered net shaping, *Mater. Lett.* 216 (2018) 16–19.
- [6] R. Wang, D. Gu, L. Xi, K. Lin, M. Guo, H. Zhang, Selective laser melted TiB₂/Ti6Al4V graded materials and first-principle calculations, *Mater. Lett.* 254 (2019) 33–36.
- [7] Y. Zhang, A. Bandyopadhyay, Direct fabrication of compositionally graded Ti-Al₂O₃ multi-material structures using Laser Engineered Net Shaping, *Addit. Manuf.* 21 (2018) 104–111.
- [8] D.C. Hofmann, S. Roberts, R. Otis, J. Kolodziejaska, R.P. Dillon, J.O. Suh, A. Shapiro, Z.K. Liu, J.P. Borgonia, Developing gradient metal alloys through radial deposition additive manufacturing, *Sci. Rep.* 4 (2014) 5357.
- [9] H. Sahasrabudhe, R. Harrison, C. Carpenter, A. Bandyopadhyay, Stainless steel to titanium bimetallic structure using LENS™, *Addit. Manuf.* 5 (2015) 1–8.
- [10] I. Tomashchuk, P. Sallamand, N. Belyavina, M. Pilloz, Evolution of microstructures and mechanical properties during dissimilar electron beam welding of titanium alloy to stainless steel via copper interlayer, *Mater. Sci. Eng., A* 585 (2013) 114–122.
- [11] O. Yilmaz, H. Çelik, Electrical and thermal properties of the interface at diffusion-bonded and soldered 304 stainless steel and copper bimetal, *J. Mater. Process. Technol.* 141 (1) (2003) 67–76.
- [12] D. Manesh, K. Taheri, An investigation of deformation behavior and bonding strength of bimetal strip during rolling, *Mech. Mater.* 37 (5) (2005) 531–542.
- [13] B.V. Krishna, P. Venugopal, K.P. Rao, Co-extrusion of dissimilar sintered P/M preforms—an explored route to produce bimetallic tubes, *Mater. Sci. Eng., A* 407 (1–2) (2005) 77–83.
- [14] A. Durgutlu, H. Okuyucu, B. Gulenc, Investigation of effect of the stand-off distance on interface characteristics of explosively welded copper and stainless steel, *Mater. Des.* 29 (7) (2008) 1480–1484.
- [15] M.H. Bina, F. Dehghani, M. Salimi, Effect of heat treatment on bonding interface in explosive welded copper/stainless steel, *Mater. Des.* 45 (2013) 504–509.
- [16] S. Guo, Q. Zhou, J. Kong, Y. Peng, Y. Xiang, T. Luo, K. Wang, J. Zhu, Effect of beam offset on the characteristics of copper/304stainless steel electron beam welding, *Vacuum* 128 (2016) 205–212.
- [17] J. Koopmann, J. Voigt, T. Niendorf, Additive manufacturing of a steel–ceramic multi-material by selective laser melting, *Metall. Mater. Trans. B* 50 (2) (2019) 1042–1051.
- [18] C. Wei, Y.-H. Chueh, X. Zhang, Y. Huang, Q. Chen, L. Li, Easy-to-remove composite support material and procedure in additive manufacturing of metallic components using multiple material laser-based powder bed fusion, *J. Manuf. Sci. Eng.* 141 (7) (2019).
- [19] B. Onuik, A. Bandyopadhyay, Additive manufacturing of Inconel 718 – Ti6Al4V bimetallic structures, *Addit. Manuf.* 22 (2018) 844–851.
- [20] L. Liu, Z. Zhuang, F. Liu, M. Zhu, Additive manufacturing of steel–bronze bimetal by shaped metal deposition: interface characteristics and tensile properties, *Int. J. Adv. Manuf. Technol.* 69 (9–12) (2013) 2131–2137.
- [21] M. Zhang, Y. Yang, D. Wang, C. Song, J. Chen, Microstructure and mechanical properties of CuSn/18Ni300 bimetallic porous structures manufactured by selective laser melting, *Mater. Des.* 165 (2019).
- [22] B. Onuik, B. Heer, A. Bandyopadhyay, Additive manufacturing of Inconel 718—copper alloy bimetallic structure using laser engineered net shaping (LENS™), *Addit. Manuf.* 21 (2018) 133–140.
- [23] J. Chen, Y. Yang, C. Song, M. Zhang, S. Wu, D. Wang, Interfacial microstructure and mechanical properties of 316L /CuSn10 multi-material bimetallic structure fabricated by selective laser melting, *Mater. Sci. Eng., A* 752 (2019) 75–85.
- [24] Y. Chivel, New approach to multi-material processing in selective laser melting, *Phys. Procedia* 83 (2016) 891–898.
- [25] Peter Regenfuss, Robby Ebert, Horst Exner, Laser micro sintering—a versatile instrument for the generation of microparts, *Laser Tech. J.* 4 (1) (2007) 26–31.
- [26] A.G. Demir, B. Previtali, Multi-material selective laser melting of Fe/Al-12Si components, *Manuf. Lett.* 11 (2017) 8–11.
- [27] C. Wei, Z. Sun, Y. Huang, L. Li, Embedding anti-counterfeiting features in metallic components via multiple material additive manufacturing, *Addit. Manuf.* 24 (2018) 1–12.
- [28] Z. Mao, D.Z. Zhang, J. Jiang, G. Fu, P. Zhang, Processing optimisation, mechanical properties and microstructural evolution during selective laser melting of Cu-15Sn high-tin bronze, *Mater. Sci. Eng., A* 721 (2018) 125–134.
- [29] J. Suryawanshi, K.G. Prashanth, U. Ramamurty, Mechanical behavior of selective laser melted 316L stainless steel, *Mater. Sci. Eng., A* 696 (2017) 113–121.
- [30] Z.H. Liu, D.Q. Zhang, S.L. Sing, C.K. Chua, L.E. Loh, Interfacial characterization of SLM parts in multi-material processing: metallurgical diffusion between 316L stainless steel and C18400 copper alloy, *Mater. Char.* 94 (2014) 116–125.
- [31] C. Wei, Z. Sun, Q. Chen, Z. Liu, L. Li, Additive manufacturing of horizontal and 3D functionally graded 316L/Cu10Sn components via multiple material selective laser melting, *J. Manuf. Sci. Eng.* 141 (8) (2019).

- [32] J.P. Kruth, L. Froyen, J. Van Vaerenbergh, P. Mercelis, M. Rombouts, B. Lauwers, Selective laser melting of iron-based powder, *J. Mater. Process. Technol.* 149 (1–3) (2004) 616–622.
- [33] A. Simchi, Direct laser sintering of metal powders: mechanism, kinetics and microstructural features, *Mater. Sci. Eng., A* 428 (1–2) (2006) 148–158.
- [34] I. Yadroitsev, P. Bertrand, I. Smurov, Parametric analysis of the selective laser melting process, *Appl. Surf. Sci.* 253 (19) (2007) 8064–8069.
- [35] I. Yadroitsev, A. Gusarov, I. Yadroitsava, I. Smurov, Single track formation in selective laser melting of metal powders, *J. Mater. Process. Technol.* 210 (12) (2010) 1624–1631.
- [36] W. Di, Y. Yongqiang, S. Xubin, C. Yonghua, Study on energy input and its influences on single-track, multi-track, and multi-layer in SLM, *Int. J. Adv. Manuf. Technol.* 58 (9–12) (2011) 1189–1199.
- [37] H.-J. Lee, T. Cagin, W.L. Johnson, W.A. Goddard, Criteria for formation of metallic glasses: the role of atomic size ratio, *J. Chem. Phys.* 119 (18) (2003) 9858–9870.
- [38] Characterization of explosively bonded iron and copper plates.pdf>. Livne Z, Munitz A, Characterization of explosively bonded iron and copper plates, *J. Mater. Sci.* 22 (4) (1987) 1495–1500.
- [39] C. Tan, K. Zhou, W. Ma, L. Min, Interfacial characteristic and mechanical performance of maraging steel-copper functional bimetal produced by selective laser melting based hybrid manufacture, *Mater. Des.* 155 (2018) 77–85.
- [40] K.D. Leedy, James F. Stubbins, Copper alloy–stainless steel bonded laminates for fusion reactor applications: tensile strength and microstructure, *Mater. Sci. Eng., A* 297 (1–2) (2001) 10–18.
- [41] B.M. RK, P. Maji, A. Samadhiya, S.K. Ghosh, B.S. Roy, A.K. Das, S.C. Saha, A study on induction welding of mild steel and copper with flux under applied load condition, *J. Manuf. Process.* 34 (2018) 435–441.
- [42] Y. Zhang, J. Huang, H. Chi, N. Cheng, Z. Cheng, S. Chen, Study on welding– brazing of copper and stainless steel using tungsten/metal gas suspended arc welding, *Mater. Lett.* 156 (2015) 7–9.
- [43] M. Sahul, M. Sahul, M. Turia, P. Zacková, Disk laser welding of copper to stainless steel, *Adv. Mater. Res.* 1077 (2014) 76–81.
- [44] A. Durgutlu, B. Güleç, F. Findik, Examination of copper/stainless steel joints formed by explosive welding, *Mater. Des.* 26 (6) (2005) 497–507.
- [45] D. Zhang, D. Qiu, M.A. Gibson, Y. Zheng, H.L. Fraser, D.H. StJohn, M.A. Easton, Additive manufacturing of ultrafine-grained high-strength titanium alloys, *Nature* 576 (7785) (2019) 91–95.
- [46] X. Zhou, K. Li, D. Zhang, X. Liu, J. Ma, W. Liu, Z. Shen, Textures formed in a CoCrMo alloy by selective laser melting, *J. Alloys Compd.* 631 (2015) 153–164.
- [47] L. Thijs, M.L. Montero Sistiaga, R. Wauthle, Q. Xie, J.-P. Kruth, J. Van Humbeeck, Strong morphological and crystallographic texture and resulting yield strength anisotropy in selective laser melted tantalum, *Acta Mater.* 61 (12) (2013) 4657–4668.
- [48] A. Aggarwal, S. Patel, A. Kumar, Selective laser melting of 316L stainless steel: physics of melting mode transition and its influence on microstructural and mechanical behavior, *JOM (J. Occup. Med.)* 71 (3) (2018) 1105–1116.
- [49] Y. Liu, Z. Pang, J. Zhang, Comparative study on the influence of subsequent thermal cycling on microstructure and mechanical properties of selective laser melted 316L stainless steel, *Appl. Phys. A* 123 (11) (2017).
- [50] S.N. Dub, Y.Y. Lim, M.M. Chaudhri, Nanohardness of high purity Cu (111) single crystals: the effect of indenter load and prior plastic sample strain, *J. Appl. Phys.* 107 (4) (2010).